NANO LETTERS
Letter
pubs.acs.org/NanoLett

Propagating Nanocavity-Enhanced Rapid Crystallization of Silicon Thin Films

Andrew J. Wagner,[†] Curtis M. Anderson,[‡,§] Jason N. Trask,[‡] Lin Cui,[‡] Alexander Chov,[†] K. Andre Mkhoyan,*,[†] and Uwe R. Kortshagen*,[‡]

[†]Department of Chemical Engineering and Materials Science and [‡]Department of Mechanical Engineering, University of Minnesota, Minneapolis, Minnesota 55455, United States

Ⓢ *Supporting Information*

ABSTRACT: We demonstrate a mechanism of solid-phase crystallization (SPC) enabled by nanoscale cavities formed at the interface between an hydrogenated amorphous silicon film and embedded 30 to 40 nm Si nanocrystals. The nanocavities, 10 to 25 nm across, have the unique property of an internal surface that is part amorphous and part crystalline, enabling capillarity-driven diffusion from the amorphous to the crystalline domain. The nanocavities propagate rapidly through the amorphous phase, up to five times faster than the SPC growth rate, while "pulling behind" a crystalline tail. Using transmission electron microscopy it is shown that twin boundaries exposed on the crystalline surface accelerate crystal growth and influence the direction of nanocavity propagation.

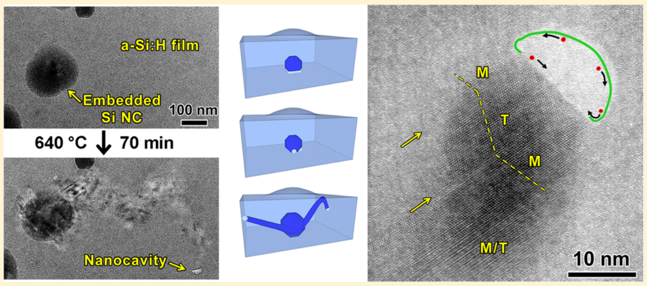

KEYWORDS: *Amorphous silicon, solid-phase crystallization, transmission electron microscopy, nanocavities, nanocrystals*

Crystallization of amorphous thin films is a ubiquitous approach to producing polycrystalline thin films of many materials.[1−8] Among the numerous processes developed, solid-phase crystallization (SPC) produces films with excellent purity, high density, and good conformity. SPC proceeds by growth of small crystallites that nucleate in the amorphous matrix during a lengthy incubation period of a few hours or more at temperatures greater than 600 °C for thin film hydrogenated amorphous silicon (a-Si:H). Numerous methods overcome the thermal and temporal limitations of traditional SPC, however each is associated with its own drawbacks such as high film porosity, the incorporation of metallic impurities, or the impracticality for large-scale application.[9−12]

Incorporation of crystalline seeds into an a-Si:H film can substantially reduce crystallization time by providing heterogeneous nucleation sites.[13,14] However, the existing approaches to introducing seeds offer limited control over seed size and aerial density. To overcome this challenge, we designed and constructed a dual-plasma reactor in which large silicon nanocrystals are synthesized by a filamentary plasma, injected through an orifice into a plasma-enhanced chemical vapor deposition (PECVD) reactor, and there are embedded in a PECVD-grown a-Si:H film containing ~10 atom % hydrogen (Figure 1a) (see Supporting Information for details). The nanocrystals are highly monodisperse, 30−40 nm in size, and cubic or cuboctahedral in shape (Figure 2a,d), depending on the radiofrequency power that is applied for nanocrystal synthesis. The embedded Si nanocrystals acted as heterogeneous nucleation sites for crystal growth while annealing, reducing the crystallization time by up to 90% while providing independent film and particle synthesis (see Supporting Information).

When cuboctahedral nanocrystals were employed as seeds, we observed through transmission electron microscopy (TEM) the formation of elongated nanoscale cavities at the boundary between the amorphous film and the embedded nanocrystals while heating to a temperature of 650 °C over 15 min (Figure 1b,c). These elongated nanocavities, confirmed hollow by high-angle annular dark-field scanning TEM (HAADF-STEM) (see Supporting Information), become rounded, 5 to 30 nm across, within a few minutes (Figure 1d) and begin moving through the amorphous film, leaving behind tails of crystalline silicon that continue to grow by SPC (Figure 1e and Supporting Information Movie 1). Nanocavities propagate with speeds up to five times faster in the sample plane than the SPC growth (Figure 1f). For example, at 650 °C nanocavity speeds are between 5 nm min^{-1} and 13 nm min^{-1}, increasing linearly with cavity size, compared to measured growth velocities of 1.2 nm min^{-1} and 4.5 nm min^{-1} for the SPC slow-growth and fast-growth directions, respectively. TEM image sequences of propagating nanocavities in 120 nm films show that the shape of cavities is dynamic with time while the cavity volume appears to remain constant (see Supporting Information Movies 2 and 3).

Films containing cuboctahedral seed crystals typically exhibited one or more mobile nanocavities per seed while cubic seed crystals seldom induced cavities. To investigate the

Received: September 26, 2013
Published: October 29, 2013

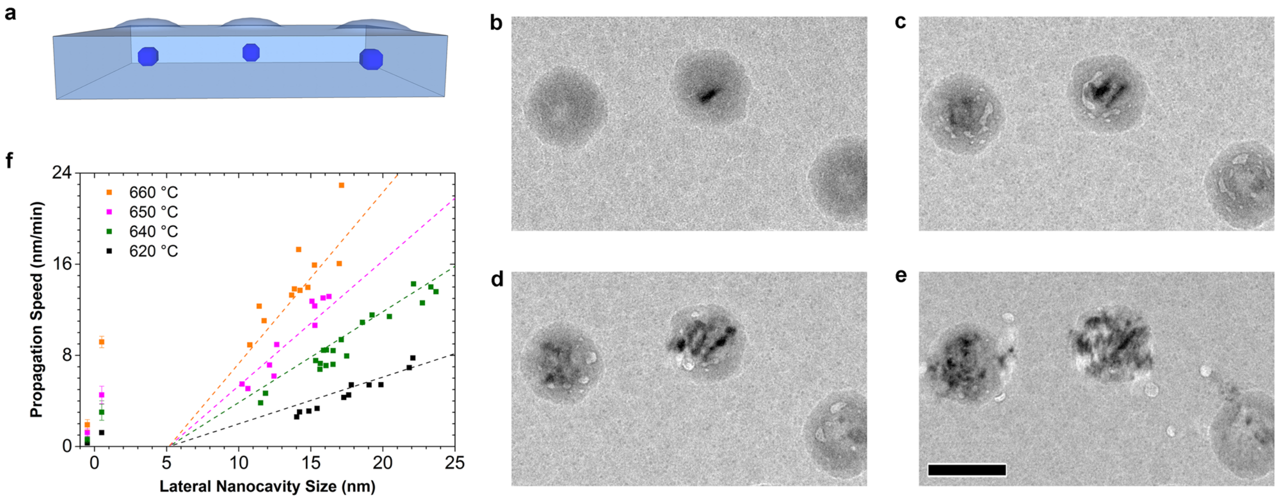

Figure 1. (a) Schematic of the a-Si:H film containing Si nanocrystals. A 20 nm bottom layer of a-S:H is deposited followed by deposition of Si nanocrystals. A 100 nm top layer of a-Si:H embeds the nanocrystals in a continuous film. (b−e) In-situ TEM image series of seeded a-Si:H film. (b) As-deposited 120 nm a-Si:H films containing 30 nm rounded Si nanocrystals. (c) Elongated cavities form near the nanocrystal seed while ramping to 640 °C in 15 min. (d) The cavities become rounded within a few minutes at the soak temperature and (e) begin moving away from the nanocrystal at a rate of 1−15 nm/min leaving behind tails of crystalline Si. (f) Growth velocities for SPC along the fast and slow axes offset from 0 nm by ±0.5 nm, respectively, and the propagation velocities for nanocavities of different size at 620−660 °C. Scale bar is 100 nm. Images were acquired after 0, 15, 18, and 25 min at a soak temperature of 640 °C.

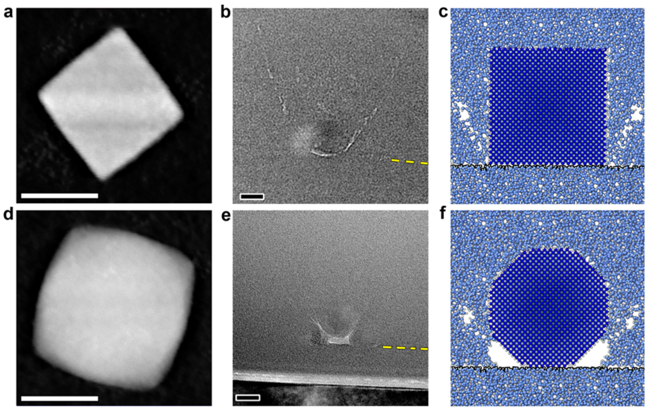

Figure 2. (a,d) HAADF-STEM images of a 31 nm cubic nanocrystal (a) and a 39 nm cuboctahedral nanocrystal (d). (b,e) Cross-section TEM images of a-Si:H films with embedded cubic and a cuboctahedral nanocrystal seeds, respectively. A parabolic porous region extends from the base of the nanocrystal seeds toward the a-Si:H surface that forms due to shadowing of the top layer deposition. Cuboctahedral seeds (e) have a more significant porosity at their bases that develop into nanocavities up to a few tens of nanometers in size upon annealing. The seeds lack well-defined boundaries due to epitaxy during deposition of the top a-Si:H layer. (c,f) Drawings of the porous region surrounding the embedded nanocrystals. Scale bars are 20 nm.

origin of the nanocavities we prepared cross sections of as-deposited films containing seed crystals. Films with embedded cubic seeds have thin parabolic regions of porous a-Si:H extending from the base of each seed crystal toward the film surface (Figure 2b). Films with embedded cuboctahedral seeds have a similar structure but with greater porosity near the base of each nanocrystal seed (Figure 2e). Shadowing by the nanocrystals during a-Si:H vapor phase deposition appears to cause cusping of the growing film that results in the formation of small pores as deposition continues.[15] The convex surface of cuboctahedral seed crystals more strongly shadows the deposition resulting in the greater porosity around the base of each nanocrystal (Figure 2c−f). During annealing, the porous regions around the nanocrystal bases appear to coalesce into larger nanocavities which by nature of their location between the crystal seeds and the amorphous phase are bound by internal surfaces that are part amorphous and part crystalline.

We propose that the lower chemical potential of atoms on the crystalline silicon surface compared to the amorphous silicon surface acts as the driving force for mass transport from the amorphous to the crystalline part of the surface. The free energy for amorphous versus crystalline Si has been studied both through experiments and simulation, reporting a difference in the range of 0.15−0.23 eV atom^{-1}.[16−18] Mobile atoms on the crystalline surface then become incorporated into the crystalline tail by epitaxy. On the basis of this proposed mechanism, we calculate the propagation speed for a nanocavity to be 15 nm min^{-1} at 640 °C using the Mullins equation for capillarity-induced diffusion along the amorphous surface,[24,25] and it is comparable to the ~10 nm min^{-1} measured experimentally (see Supporting Information). The nanocavities' speed increases with their size, as can be seen in Figure 1f, suggesting that diffusion is sufficiently fast for cavity propagation. If surface diffusion were the rate limiting step in the nanocavity propagation, the nanocavity speed would vary inversely with nanocavity size due to the increasing crystalline surface area and an approximately linear increase in mass transfer across the a/c interface. This is reinforced by the dynamic shape of the amorphous surface over time which may result from Rayleigh-Taylor instabilities[19] owing to the growing crystal changing the a/c interface and the influence of local curvature of the amorphous surface on diffusion.

The high-resolution TEM (HR-TEM) image shown in Figure 3a provides a detailed view of the rounded amorphous surface terminating at a faceted crystalline "rear" surface. Here, the crystalline tail, aligned along its [011] zone axis relative to the incident beam, has two parallel Σ3 twin boundaries terminating on the rear of the nanocavity. The main crystal M has a $(11\bar{1})$ facet while the twinned crystal T is composed of a

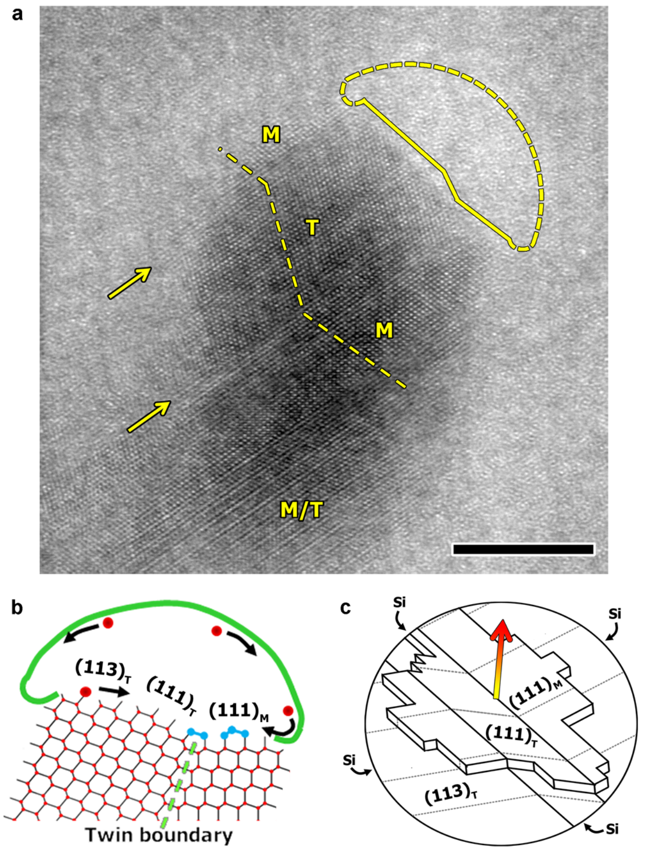

Figure 3. (a) High-resolution TEM image of a nanocavity along its $[1\bar{1}0]$ zone axis. Two $\Sigma 3\{111\}$ twin boundaries, indicated by yellow arrows, terminate at the rear of the nanocavity. The crystalline surface contains $\{111\}_{M,T}$ and $\{113\}_T$ facets. (b,c) Schematics of a crystalline surface containing one twin. Diffusion of surface atoms across the free energy landscape ends in attachment and growth of the crystalline surface, accelerated by preferential nucleation sites along the exposed twin boundary. Scale bar is 10 nm.

small $(11\bar{1})$ and larger $(\bar{3}11)$ facet. HR-TEM image analysis of many nanocavities showed that the facets are predominately $\{111\}$ and $\{113\}$. Further behind the nanocavity is a region with a superstructure, periodicity $3d_{(111)}$, characteristic of superposed crystals related by twinning parallel to the electron optic axis.[20]

Twinning is known to influence crystallization in silicon. The low-energy, slow-growth $\{111\}$ surfaces often develop stacking faults and twin boundaries due to a low stacking fault energy of about 0.03 eV atom^{-1}.[21] Re-entrant twin boundaries exposed on a crystalline surface create preferential nucleation sites that accelerate growth along the $\langle 11\bar{2}\rangle$ direction while preserving low-energy $\{111\}$ surfaces on each side of the twin boundary.[22,23] The presence of twins in the crystalline tail, terminating on the cavity's crystalline surface, suggests that nanocavity propagation is mediated by step nucleation at twin boundaries (Figure 3b,c), which is consistent with the observation of directional nanocavity propagation where a crystalline tail contains multiple segments of linear growth (Figure 4a–e). Analysis of dark-field TEM (DF-TEM) images and convergent-beam electron diffraction (CBED) patterns of crystalline tails indicate the same (see Supporting Information).

Nanocavity propagation speed mediated by the presence of twin boundaries is expected to be dependent on length and number of exposed twin boundaries as depicted in Figure 4f–g. In crystals grown by SPC, twin boundaries are typically separated by 1–20 nm,[24] consistent with our observation of twin boundary spacing within the tails. Small nanocavities may not have twin boundaries on their crystalline surface and therefore not have accelerated growth. The length of twin boundaries will also be dependent on position and generally shorter than the nanocavity size. Additionally, twin boundaries not oriented precisely along the propagation direction will grow across the cavity and into the amorphous matrix and thus no longer contribute to cavity propagation but instead to twin-mediated SPC at the a/c interface. The result is that larger nanocavities, having greater twin boundary length and therefore more nucleation sites, will propagate faster than smaller cavities. Nanocavity propagation will be fastest when directed along the $\langle 112\rangle$ direction of the active twin plane as a single re-entrant edge can continuously support crystal growth. Changes in propagation direction can occur if a new twin boundary develops on exposed $\{111\}$ surfaces.

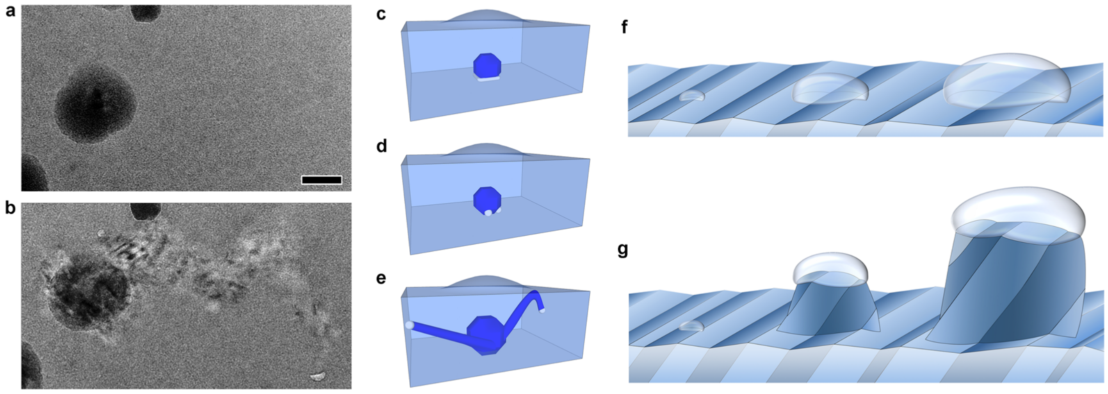

Figure 4. Plan-view BF-TEM image of embedded Si nanocrystal seeds in a-Si:H (a) as-deposited and (b) after annealing for 70 min at 640 °C. The nanocavity has propagated approximately 1 μm leaving behind it a crystalline tail. (c–e) A cartoon of the film evolution while annealing. A porous region near the base of the seed coalesces into tens-of-nanometer-sized nanocavities at elevated temperature. The cavity surface, part amorphous and part crystalline, promotes mass transfer from the amorphous to the crystalline domain. The receding amorphous surface and growing crystalline surface creates a crystalline tail as the nanocavity propagates through the film. (f,g) A cartoon showing nanocavities of different size at an a/c interface. The larger cavities, possessing greater twin boundary length, propagate faster leading to formation of crystalline tails over time. Scale bar is 100 nm.

The nanocavity propagation speeds can be described by size-dependent Arrhenius equation

$$\nu_{\mathrm{NC}}(R, T) = \upsilon_0 \frac{d_{112}(R - R_c)}{d_{110}} \exp\left(\frac{-E_A}{k_B T}\right) \quad (1)$$

where d_{112} and d_{110} are the {112} and {110} planar spacings, ν_0 is the vibrational attempt frequency, R is the nanocavity size, R_c is a critical cavity size below which enhanced crystallization does not occur, E_A is an effective activation energy, k_B is the Boltzmann constant, and T is temperature. Here d_{112} accounts for surface step height per nucleation event and d_{110} normalizes for the number of nucleation sites. The critical size R_c results from the temporal averaged twin boundary length exposed on the nanocavity surface. Using the Levenberg–Marquardt fitting algorithm[25] to fit eq 1 to experimental data (Figure 1f) with an attempt frequency of $\nu_0 = 10^{13}$ Hz,[26] we find an activation energy of $E_A = 2.33 \pm 0.01$ eV and a critical size of $R_c = 5.15 \pm 0.60$ nm. The activation energy only weakly depends on attempt frequency (see Supporting Information). As growth appears to be limited by nucleation of new terraces, this activation energy can be considered as that for nucleation at a twin boundary.

Because of the rapid movement of nanocavities through the film, leading to fast growth of crystalline tails, a significant improvement of the crystallization kinetics should be expected. Raman spectroscopy studies of the crystallization revealed reductions in characteristic crystallization time of 90% for 100 nm a-Si:H films containing cuboctahedral Si nanocrystals, respectively. To develop a model for the benefits of such nanocavity-induced crystallization for thicker films we modified the Johnson–Mehl–Avrami–Kolmogorov (JMAK) model for crystal fraction (see Supporting Information) to account for spherulitic growth of nanocrystal seeds and a single crystalline tail modeled as a cone extending from each nanocrystal seed to a nanocavity. Applying the experimental SPC growth velocity and nanocavity propagation speeds obtained from heated-stage TEM experiments, we compared the time required to crystallize a 1 μm film containing a layer of nanocrystal seeds. The model is consistent with experimental results in that the presence of nanocrystal seeds reduced the characteristic crystallization time by more than 80%. The addition of nanocavities reduced the crystallization time by another 50% (see Supporting Information). This can be further optimized by tuning the density and location of nanocrystals within the film.

To our knowledge this is the first demonstration of a crystallization process perpetuated by diffusion along an enclosed surface. The surface of nanocavities located at an *a*/*c* interface have a chemical potential gradient along which atoms diffuse, resulting in a receding front amorphous surface and a growing rear crystalline surface. Twin boundaries on the crystalline surface provide preferential nucleation sites which accelerate growth and create a preferential growth direction. As the nanocavities propagate through the film a crystalline tail develops, creating a rapidly expanding *a*/*c* interface surface that crystallizes the surrounding film by SPC. The result is a dramatic reduction in crystallization time for amorphous Si films. Beyond the potential for enhancing crystallization in silicon films, the kinetics of this process should translate to the crystallization of many other materials.

Methods. *Seeded a-Si:H Film Growth.* Films were grown layer-by-layer in a dual-plasma reactor consisting of a parallel-plate PECVD chamber for a-Si:H growth and a flow-through plasma reactor[27] for nanocrystal synthesis. The nanocrystal reactor is positioned directly above the PECVD chamber and separated by a pressure-reducing orifice (see Supporting Information). a-Si:H was grown with a substrate temperature of 250 °C, gas flow of 40 standard cubic centimeter per minute (sccm) 5% SiH_4 in He balance, chamber pressure of 15 Pa, and radiofrequency (rf) power density of 3.6 mW cm^{-2} giving a deposition rate of 1.6 nm/min. The Si nanocrystal reactor consists of a glass tube terminated by grounded ultratorr fittings and a ring electrode. A 1 mm orifice separates the reactor from high vacuum. A gas flow of 3 sccm 5% SiH_4 in He balance and 4 sccm Ar creates a pressure of 340 Pa. A plasma discharge is created by an applied rf power of 130 W for cubic nanocrystals and 150 W for cuboctahedral nanocrystals.

Specimen Preparation. Films for plan-view TEM were deposited directly onto carbon-coated molybdenum grids (Grid-Tech Mo-400HD) and consisted of a 20 nm bottom layer of a-Si:H, a layer of seed crystals with typical density of 1 to 5 seeds μm^{-2}, and a 100 nm top layer of a-Si:H. Films for cross-section TEM were deposited on Si(100) "mesas" (Hysitron Inc., #5-0923) and prepared by a liftout-free focused ion beam method using a FEI Quanta 3D 200, detailed in the Supporting Information.

Characterization. Heated-stage TEM was performed using a Gatan 652 double-tilt heating holder in an FEI Tecnai G2 F30 (S)TEM with TWIN pole piece operating at 100 keV and equipped with a Gatan 4k × 4k Ultrascan CCD. HR-TEM and STEM-ADF imaging was performed in an FEI Tecnai G2 F30 (S)TEM with S-TWIN pole piece operating at 100 and 200 kV, respectively.

Heating in the TEM. Temperature was ramped to 650 °C at a rate between 35 and 45 °C min^{-1}, held for one minute, and then set to the soak temperature. Images were acquired every 11 s. SPC growth velocity and nanocavity propagation speeds were measured every third frame, 33 s apart. Fast-growth SPC was identified by elongated crystals extending from the nanocrystal seeds while slow-growth was measured as the expansion of seed crystals having slow, isotropic growth. Nanocavity propagation speed was measured as the displacement of the crystalline surface between frames. When no well-defined crystalline surface was visible, displacements were recorded but excluded from measurement.

■ ASSOCIATED CONTENT

Ⓢ Supporting Information

Detailed experimental methods, analysis of crystalline tails, Arrhenius fitting of nanocavity propagation, analysis of film crystallization rates, and in situ TEM movies of nanocavity formation and propagation. This material is available free of charge via the Internet at http://pubs.acs.org.

■ AUTHOR INFORMATION

Corresponding Authors

*E-mail: (K.A.M.) mkhoyan@umn.edu.
*E-mail: (U.R.K.) kortshagen@umn.edu.

Present Address

[§]Delaware Research and Technology Center, Air Liquide, Delaware, United States.

Author Contributions

A.J.W. performed materials synthesis, characterization, analysis, and produced the manuscript. C.M.A. performed early experiments and characterization. J.T. and L.C. assisted in synthesis and characterization. A.C. assisted in characterization. K.A.M. and U.R.K. provided guidance, analysis, and edited the manuscript.. All authors have given approval to the final version of the manuscript.

Notes

The authors declare no competing financial interest.

■ ACKNOWLEDGMENTS

This work was partially supported by MRSEC Program of the National Science Foundation under Award Number DMR-0819885, NSF Grant DMR-0705675 and by the Xcel Energy Renewable Development Fund under Grant RD-3-25. Parts of this work were carried out in the Characterization Facility, University of Minnesota, which receives partial support from NSF through the MRSEC program. A.J.W. would like to thank Jason Myers, Richard Liptak, Wei Zhang, and Lance Wheeler of the University of Minnesota for their assistance and fruitful discussions.

■ ABBREVIATIONS

a-Si:H, hydrogenated amorphous silicon; TEM, transmission electron microscope; HAADF-STEM, high-angle annular dark-field scanning TEM; DF-TEM, dark-field TEM; CBED, convergent-beam electron diffraction; HR-TEM, high-resolution TEM; SPC, solid-phase crystallization; plasma-enhanced chemical vapor deposition, PECVD

■ REFERENCES

(1) Sun, Y.; Rogers, J. A. Inorganic semiconductors for flexible electronics. *Adv. Mater.* **2007**, *19* (15), 1897−1916.

(2) Dunand, D. C.; Müllner, P. Size effects on magnetic actuation in Ni-Mn-Ga shape-memory alloys. *Adv. Mater.* **2011**, *23* (2), 216−232.

(3) Striemer, C. C.; Gaborski, T. R.; McGrath, J. L.; Fauchet, P. M. Charge- and size-based separation of macromolecules using ultrathin silicon membranes. *Nature* **2007**, *445* (7129), 749−753.

(4) Kirihara, A.; Uchida, K. I.; Kajiwara, Y.; Ishida, M.; Nakamura, Y.; Manako, T.; Saitoh, E.; Yorozu, S. Spin-current-driven thermoelectric coating. *Nat. Mater.* **2012**, *11* (8), 686−689.

(5) Bi, L.; Hu, J.; Jiang, P.; Kim, D. H.; Dionne, G. F.; Kimerling, L. C.; Ross, C. A. On-chip optical isolation in monolithically integrated non-reciprocal optical resonators. *Nat. Photonics* **2011**, *5* (12), 758−762.

(6) Scherrer, B.; Heiroth, S.; Hafner, R.; Martynczuk, J.; Bieberle-Hütter, A.; Rupp, J. L. M.; Gauckler, L. J. Crystallization and microstructure of yttria-stabilized-zirconia thin films deposited by spray pyrolysis. *Adv. Funct. Mater.* **2011**, *21* (20), 3967−3975.

(7) Miikkulainen, V.; Leskelä, M.; Ritala, M.; Puurunen, R. L. Crystallinity of inorganic films grown by atomic layer deposition: Overview and general trends. *J. Appl. Phys.* **2013**, *113* (2), 021301.

(8) Longo, V.; Verheijen, M. A.; Roozeboom, F.; Kessels, W. M. M. Crystallization study by transmission electron microscopy of $SrTiO_3$ thin films prepared by plasma-assisted ALD. *ECS J. Solid State Sci. Technol.* **2013**, *2* (5), N120−N124.

(9) Jang, J.; Oh, J. Y.; Kim, S. K.; Choi, Y. J.; Yoon, S. Y.; Kim, C. O. Electric-field-enhanced crystallization of amorphous silicon. *Nature* **1998**, *395* (6701), 481−483.

(10) Radnoczi, G.; Robertsson, A.; Hentzell, H. T. G.; Gong, S. F.; Hasan, M. A. Al induced crystallization of a-Si. *J. Appl. Phys.* **1991**, *69* (9), 6394−6399, DOI: 10.1063/1.348842.

(11) Im, J. S.; Kim, H. J.; Thompson, M. O. Phase transformation mechanisms involved in excimer laser crystallization of amorphous silicon films. *Appl. Phys. Lett.* **1993**, *63* (14), 1969−1971.

(12) Shah, A. V.; Meier, J.; Vallat-Sauvain, E.; Wyrsch, N.; Kroll, U.; Droz, C.; Graf, U. Material and solar cell research in microcrystalline silicon. *Sol. Energy Mater. Sol. Cells* **2003**, *78* (1−4), 469−491.

(13) Bertran, E.; Sharma, S. N.; Viera, G.; Costa, J.; St'ahel, P.; Cabarrocas, P. R. I. Effect of the nanoparticles on the structure and crystallization of amorphous silicon thin films produced by rf glow discharge. *J. Mater. Res.* **1998**, *13* (9), 2476−2479.

(14) Mattoni, A.; Colombo, L. Crystallization kinetics of mixed amorphous-crystalline nanosystems. *Phys. Rev. B* **2008**, *78* (7), 075408.

(15) Smith, D. L. *Thin-film deposition: Principles and practice*; McGraw-Hill: New York, 1995.

(16) Hara, S.; Izumi, S.; Kumagai, T.; Sakai, S. Surface energy, stress and structure of well-relaxed amorphous silicon: A combination approach of ab initio and classical molecular dynamics. *Surf. Sci.* **2005**, *585* (1−2), 17−24.

(17) Pan, B. C.; Biswas, R. Structure and simulation of hydrogenated nanocrystalline silicon. *J. Appl. Phys.* **2004**, *96* (11), 6247−6252.

(18) Donovan, E. P.; Spaepen, F.; Turnbull, D.; Poate, J. M.; Jacobson, D. C. Heat of crystallization and melting point of amorphous silicon. *Appl. Phys. Lett.* **1983**, *42*, 698−700.

(19) Glaeser, A. M. Model studies of Rayleigh instabilities via microdesigned interfaces. *Interface Sci.* **2001**, *9* (1−2), 65−82.

(20) Cayron, C.; Den Hertog, M.; Latu-Romain, L.; Mouchet, C.; Secouard, C.; Rouviere, J. L.; Rouviere, E.; Simonato, J. P. Odd electron diffraction patterns in silicon nanowires and silicon thin films explained by microtwins and nanotwins. *J. Appl. Crystallogr.* **2009**, *42* (2), 242−252.

(21) Gilman, J. J. Direct measurements of the surface energies of crystals. *J. Appl. Phys.* **1960**, *31* (12), 2208−2218.

(22) Wagner, R. S. On the growth of germanium dendrites. *Acta Metall.* **1960**, *8* (1), 57−60.

(23) Drosd, R.; Washburn, J. Some observations on the amorphous to crystalline transformation in silicon. *J. Appl. Phys.* **1982**, *53* (1), 397−403.

(24) Batstone, J. L. Insitu crystallization of amorphous-silicon in the transmission electron-microscope. *Philos. Mag. A* **1993**, *67* (1), 51−72.

(25) Nocedal, J.; Wright, S. *Numerical optimization*; Springer: New York, 2006.

(26) Venables, J. A. Atomic processes in crystal growth. *Surf. Sci.* **1994**, *299−300* (0), 798−817.

(27) Bapat, A.; Anderson, C.; Perrey, C. R.; Carter, C. B.; Campbell, S. A.; Kortshagen, U. Plasma synthesis of single-crystal silicon nanoparticles for novel electronic device applications. *Plasma Phys. Controlled Fusion* **2004**, *46* (12 B), B97−B109.